Journal of Rock Mechanics and Geotechnical Engineering 16 (2024) 470–482

Contents lists available at ScienceDirect

Journal of Rock Mechanics and Geotechnical Engineering

journal homepage: www.jrmge.cn

Full Length Article

Analysis of pressure response at an observation well against pressure build-up by early stage of CO_2 geological storage project

Qiang Sun [a,*], Kyuro Sasaki [b], Qinxi Dong [a,c,**], Zhenni Ye [a], Hui Wang [a], Huan Sun [a]

[a] School of Civil Engineering and Architecture, Hainan University, Haikou, 570228, China
[b] Faculty of Engineering, Kyushu University, 744 Motooka, Nishi-ku, Fukuoka, 819-0385, Japan
[c] Key Laboratory of Equipment Safety and Intelligent Technology for Guangzhou Rail Transit System, Guangzhou, 510430, China

ARTICLE INFO

Article history:
Received 6 December 2022
Received in revised form
14 February 2023
Accepted 12 March 2023
Available online 22 April 2023

Keywords:
CO_2 storage
Saline aquifer
Observation well
Pressure response
CO_2 saturation

ABSTRACT

To ensure a safe and stable CO_2 storage, pressure responses at an observation well are expected to be an important and useful field monitoring item to estimate the CO_2 storage behaviors and the aquifer parameters during and after injecting CO_2, because it can detect whether the injected CO_2 leaks to the ground surface or the bottom of the sea. In this study, pressure responses were simulated to present design factors such as well location and pressure transmitter of the observation well. Numerical simulations on the pressure response and the time-delay from pressure build-up after CO_2 injection were conducted by considering aquifer parameters and distance from the CO_2 injection well to an observation well. The measurement resolution of a pressure transmitter installed in the observation well was presented based on numerical simulation results of the pressure response against pressure build-up at the injection well and CO_2 plume front propagations. Furthermore, the pressure response at an observation well was estimated by comparing the numerical simulation results with the curve of CO_2 saturation and relative permeability. It was also suggested that the analytical solution can be used for the analysis of the pressure response tendency using pressure build-up and dimensionless parameters of hydraulic diffusivity. Thus, a criterion was established for selecting a pressure transducer installed at an observation well to monitor the pressure responses with sufficient accuracy and resolution, considering the distance from the injection well and the pressure build-up at the injection well, for future carbon capture and storage (CCS) projects.

© 2024 Institute of Rock and Soil Mechanics, Chinese Academy of Sciences. Production and hosting by Elsevier B.V. This is an open access article under the CC BY-NC-ND license (http://creativecommons.org/licenses/by-nc-nd/4.0/).

1. Introduction

The average atmospheric CO_2 concentration had increased from 280 ppm in industrial era to 411 ppm in May 2019 (Lake and Lomax, 2019). The average CO_2 concentration is increasing continuously by more than 2 ppm/year (Metz et al., 2005). With this growth rate, it will exceed 450 ppm within the next 20 years (Li et al., 2019), and the mean global temperature will increase by over 2 °C. To mitigate the increasing rate, many intergovernmental organizations have assessed climate change and exchange technology for reducing the anthropogenic CO_2 emissions (Metz et al., 2005; Shackley et al., 2005; IEAGHG, 2010). In 2017, a possible framework to reduce CO_2 emissions into the atmosphere had been agreed upon countries that joined COP23 (Obergassel et al., 2018).

CO_2 capture and geological storage is a promising way to mitigate CO_2 emissions into the atmosphere by capturing CO_2 gases from relatively large industrial sources, such as power plants, and then transporting and injecting them into porous and permeable storage reservoirs. A suitable reservoir should be covered by sealing layers with very low permeability to prevent CO_2 leakage from storage reservoirs to the ground surface or sea bottom. Three main underground storage reservoirs have been identified: saline aquifers, depleted oil and gas reservoirs, and unminable coal seams (Yang et al., 2010). Deep saline aquifers at depths over −800 m have been considered ideal because of their large storage capacity and broad distribution worldwide. The saline aquifers are permeable geologic layers located 1000–3000 m deep and can store injected CO_2 in a supercritical state under reservoir conditions.

* Corresponding author.
** Corresponding author. School of Civil Engineering and Architecture, Hainan University, Haikou, 570228, China.
E-mail addresses: 184059@hainanu.edu.cn (Q. Sun), dongqinxi@hainanu.edu.cn (Q. Dong).

Peer review under responsibility of Institute of Rock and Soil Mechanics, Chinese Academy of Sciences.

https://doi.org/10.1016/j.jrmge.2023.03.013
1674-7755 © 2024 Institute of Rock and Soil Mechanics, Chinese Academy of Sciences. Production and hosting by Elsevier B.V. This is an open access article under the CC BY-NC-ND license (http://creativecommons.org/licenses/by-nc-nd/4.0/).

The International Energy Agency (IEA) has estimated the potential contribution of carbon capture and storage (CCS) in mitigating global CO_2 emission to be as high as 20% of the global emissions in 2050, which follows the most important contribution by improvement in energy efficiency (Lipponen et al., 2011). The Blue Map reduction plan has been considered necessary to continue annual geological storage of 9.5 Gt-CO_2 by CCS for 45 years. Several ongoing pilots and commercial CCS projects have suggested that CO_2 geological storage in deep sedimentary formations is technologically feasible (Eiken et al., 2011; Hansen et al., 2013; Tanaka et al., 2014). To make a significant contribution to the mitigations of climate change, many CCS projects with larger CO_2 injection rates from an injection well need to be planned and implemented. However, the CO_2 reduction rate by CCS projects is currently limited because sufficient CCS projects have not been implemented owing to economic issues as well as social acceptance issues related to storage safety and stability.

CO_2 injections induce a pressure increase in the reservoir from its original geomechanical pressure. A large CO_2 injection rate can easily cause considerable pressure build-up in the bottom hole and its surrounding region in the reservoir, where activated faults through the upper sealing layers may lead to CO_2 leakage (Rutqvist, 2012; Mathias et al., 2014; Harp et al., 2017; González-Nicolás et al., 2019). Therefore, the management of the bottom hole pressure (BHP) as an induced pressure build-up will be a critical factor in the safe operation of CO_2 storage (Buscheck et al., 2012; Yang et al., 2018; Zheng et al., 2022). For instance, the In Salah CCS project in Algeria has shown significant geomechanical changes because of the injection pressure and site-specific geomechanical conditions. Although the injection rate of the In Salah CCS project was 1 Mt/year, the project was still shut down because of concerns about the integrity of the seal layers (Eiken et al., 2011; Goertz-Allmann et al., 2014). In the Tubåen Formation in the Snøhvit field (offshore Norway), Statoil successfully injected 1.6 Mt of CO_2 from April 2008 to April 2011. However, the CO_2 injection had to be stopped owing to an increase in pore pressure before reaching the full storage capacity of the Tubåen Formation (Hansen et al., 2013). It is easy to induce tremendous pressure build-up in the reservoir at a large injection rate. All the site CCS programs teach us that formation pressure monitoring and management is a key point to limit the implementation of CCS program on a commercial scale.

Generally, to confirm that the injected and stored CO_2 is in a safe and stable condition, it is necessary to grasp the behavior of CO_2 in the reservoir and to detect whether there is leakage of CO_2 out of the reservoirs or not. For example, in the Tomakomai CCS demonstration project (hereinafter Tomakomai CCS project) (Tanaka et al., 2014), five continuous monitoring items and three periodic monitoring items were operated for two aquifers at different average depths of 1150 m and 2700 m. The continuous monitoring items are temperature and pressure in two injection wells, temperature and pressure in two remote observation wells, and seismic monitoring at the ocean bottom and onshore. In contrast, the periodic monitoring items are marine environmental observations (sea water, bottom mud, and sea lives) and two-dimensional and three-dimensional seismic surveys. Specifically, two observation wells were drilled from onshore to the Moebetsu Formation (1100–1200 m in deep) and the Takinoue Formation (2400–3000 m in deep) to record continuous passive changes in aquifer pressure and temperature as well as CO_2 saturation in each formation water. The monitoring data recorded in the observation wells can be used to detect the movement of the CO_2 plume and judge the stability of stored CO_2 based on comparisons with the numerical simulation results using aquifer models. The original pressure of the Moebetsu Formation at the injection well was 9.3 MPa and the maximum BHP in the injection well that was recorded during the test injection was 10 MPa (Tanaka et al., 2014; Sato and Horne, 2018; Sawada et al., 2018). However, there is no pressure response recorded in the observation well OB-2 (Tanaka et al., 2014) which was drilled about 3000 m from the injection well in the Moebetsu Formation with installing pressure and temperature sensors. The reason for the lack of pressure response at the observation well was explained as the sensitivity of the pressure transducer is not sufficient to detect the pressure propagation from the injection well to the observation well.

Generally, observation wells are drilled to observe the aquifer with CO_2 storage. It is assumed that temperature and pressure gauges are installed in the bottom hole for continuous monitoring of the aquifer. They are used to detect the CO_2 plume front development and verify that the injected CO_2 had not leaked into shallower strata (Metz et al., 2005). Most of the observation wells are used to monitor the CO_2 plume front position (Mathieson et al., 2011; Hu et al., 2015). The In Salah CCS program used an observation well KB-5 (Durucan et al., 2011) with a distance of 1.3 km from the injection well KB-502 and analyzed the gas tracer injected together with CO_2 to examine the CO_2 plume development. The observation well KB-5 was used for detecting the CO_2 plume position, not for the pressure analysis, and it was an abandoned gas production well drilled in 1980, which was not well designed for the CCS program. In Germany, a Ketzin pilot CCS program used two observation wells (Ktzi 200 and Ktzi 202) to determine the pressure evolution during injection operation with a distance of 50 m and 112 m from the injection well Ktzi 201 (maximum injection rate 78 t-CO_2/d), respectively (Liebscher et al., 2013). If the distance between the observation wells and the injection well is extremely small, it can detect the CO_2 plume front development. However, according to some in situ experience, the greatest risk of CO_2 leakage for any geological storage project is associated with old wells and observation wells. Thus, an observation well located at a small distance from the injection well also creates a new potential pathway for CO_2 leakage to the sublayers.

Drilling a new observation well requires an additional budget and may create a new potential pathway for CO_2 leakage to the surface. Therefore, the observation well and installed sensors for measuring parameters, such as distance from the CO_2 injection well and the sensor sensitivity, should be suitably designed before drilling an observation well. In this study, we numerically investigated the pressure response at an observation well, induced by CO_2 injection at the early stage of CO_2 geological storage in a deep saline aquifer. The results can be used as reference data for designing an observation well and determining the location for installing sensors (or transmitters).

2. Aquifer model for CO_2 injection and storage

As shown in Fig. 1, a cylindrical grid system with (r, φ, z) coordinates was used to construct the reservoir model. The pressure

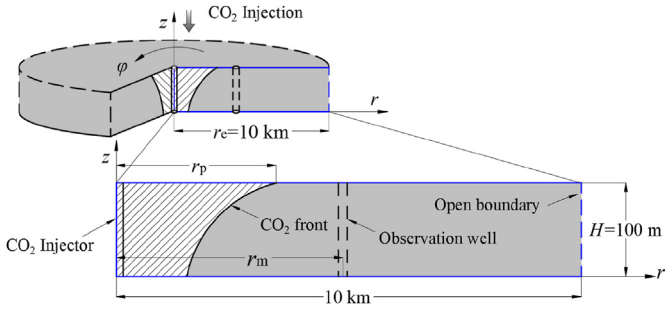

Fig. 1. Schematic aquifer model.

and CO_2 saturation distributions were simulated by injecting CO_2 from an injection well located at $r = 0$ m into an aquifer with radius r_w. It was assumed that the aquifer had uniform porosity and permeability in horizontal and vertical directions. Its outer boundary at $r = r_e$ is defined as an open boundary that the pressure is equal to the initial pressure. There is no-flow across the top and bottom boundaries. A typical aquifer model was simulated by setting $r_w = 0.1$ m and $r_e = 10$ km.

The meshing of the aquifer in the r and z directions is shown in Fig. 2. The grid blocks consist of $1000 \times 1 \times 10$ grid cells in the (r, φ, z) directions, of which 200 grid-cells were set between $r = 0.1$–400 m, and 800 grid-cells between $r = 400$–10,000 m. The reservoir consists of 10 layers with a constant spacing of 10 m in the vertical direction. CO_2 was injected from the injector into horizontal layers connecting to the aquifer by three types of perforations. The radial distance from the observation well to the injection well, r_m, was assumed to be in the range of 1000–5000 m. The pressure changes in the aquifer blocks connected to the aquifer at $r = r_m$ were considered as the pressure responses at the bottom of the observation well connected to the aquifer. Numerical simulations were conducted using the compositional reservoir simulator CMG-STARS™.

The simulation parameters for the base model are listed in Table 1. In the case of the Moebetsu Formation in the Tomakomai CCS project, the range of horizontal permeability was estimated as $k = 0.98 \times 10^{-15}$–980×10^{-15} m^2 (=1–1000 mD) from the geophysical measurements, and $k = 363 \times 10^{-15}$ m^2 (=370 mD) based on the fall-off test using the injection well after drilling. In addition, the porosity was measured as $\varphi = 0.2$–0.4 by a laboratory core test and the excavation result was $\varphi = 0.12$–0.42 (Tanaka et al., 2014). In this simulation, the uniform permeability in the horizontal direction was also set as $k = 363 \times 10^{-15}$ m^2, and the ratio of vertical permeability (k_v) to horizontal permeability (k) was $k_v/k = 0.1$. The porosity $\varphi = 0.3$ was used for the base simulations. In the present simulations, assuming that the ground surface temperature was 15 °C and geothermal gradient as 2.5–2.75 °C/100 m, the targeted aquifer temperature was 40 °C-42.5 °C, and the CO_2 injection temperature was specified as 40 °C. Therefore, the injected CO_2 was similar to the isothermal process. No geochemical reactions or mineralization were considered because a short period of fewer than 200 d was considered for simulation. In the CMG-STARS™ compositional models, the phase equilibrium is specified via phase equilibrium ratios, K–value, which is a function of gas phase pressure and temperature.

Relative permeability was modeled based on the Brooks–Corey–Burdine model (Garimella et al., 2019) and is expressed by

$$k_{rw} = S_e^{\frac{2+3\lambda}{\lambda}} \quad (1)$$

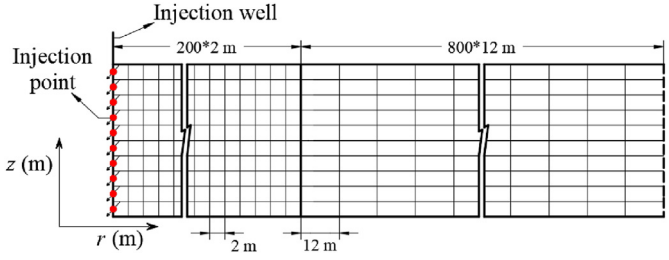

Fig. 2. Schematic diagram of meshing in the cross-section.

Table 1
Aquifer parameters and CO_2 injection well set in the base model (Tanaka et al., 2017; Sawada et al., 2018; Garimella et al., 2019).

Parameter	Present simulation	Tomakomai CCS project	Unit
Aquifer upper level	−1000	−1000–−1200	m
Aquifer thickness, H	100	100–200	m
Outer boundary radius, r_e	10,000		m
Initial aquifer pressure, p_0	10	9.3	MPa
Initial water saturation	1		
CO_2 injection temperature	40		°C
CO_2 injection pressure, $p_0 + p_i$	<14		MPa
CO_2 injection well radius, r_w	0.1		M
Porosity, φ	0.3	0.10–0.42	
Horizontal permeability, k	363×10^{-15}	363×10^{-15}	m^2
Vertical permeability, k_v	36.3×10^{-15}	36.3×10^{-15}	m^2
Rock compressibility, C_r	9×10^{-10}		Pa^{-1}
Brine water compressibility, C_w	1×10^{-10}		Pa^{-1}
$_{sc}CO_2$[a] compressibility, C_c	4×10^{-10}		Pa^{-1}
Hydraulic diffusivity, η	2.26		m^2/s

[a] $_{sc}CO_2$ denotes CO_2 in supercritical phase.

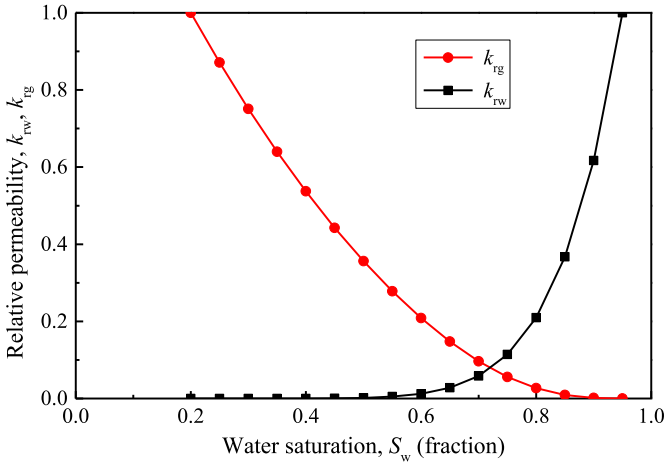

Fig. 3. Relative permeability curves used in present simulations (Brooks-Corey-Burdine model) (Garimella et al., 2019).

$$k_{rg} = \left(1 - S_e^{\frac{2+\lambda}{\lambda}}\right)(1 - S_e)^2 \quad (2)$$

$$S_e = \frac{S_w - S_{wr}}{1 - S_{wr} - S_{gr}} \quad (3)$$

where S_e is the effective saturation; k_{rw} and k_{rg} are the aqueous and gas phase relative permeabilities, respectively; S_w is the aqueous phase saturation; S_{wr} and S_{gr} are the aqueous and gas phase residual saturations, respectively; and λ is the pore size distribution index. In the present simulations, $S_{wr} = 20\%$, $S_{gr} = 5\%$, and $\lambda = 0.5$. The relative permeability curves are shown in Fig. 3. Based on the curves, the remaining water saturation after displacement of CO_2 gas is almost $S_w \approx 65\%$, which means that the CO_2 gas saturation becomes $S_g \approx 35\%$ in an aquifer except near the well.

3. Theoretical analysis

3.1. Linearized radial flow equation and estimation solution

Assuming that porous media are viscous-dominated and there is no turbulent flow, the flow in porous media can be described by Darcy's law for a single incompressible fluid phase (Hubbert, 1953):

$$\boldsymbol{q} = -\frac{k}{\mu}(\nabla p - \rho \boldsymbol{g} \nabla z) \tag{4}$$

where $\boldsymbol{q}$ is the vector of the volumetric flow rate (m^3/s); k (m^2) is the permeability; μ (Pa s) and ρ (kg/m^3) are the viscosity and density of the reservoir fluid, respectively; $\boldsymbol{g}$ is the gravitational acceleration vector directed downwards; and ∇p is the hydraulic gradient.

Without considering gravity in the vicinity of an injection well, the governing equation on pressure p (Pa) for one-dimensional radial linearized flow, assuming a constant compressibility in the aquifer, is given as (Wu and Pan, 2005):

$$\frac{\partial^2 p}{\partial r^2} + \frac{1}{r}\frac{\partial p}{\partial r} = \frac{1}{\eta}\frac{\partial p}{\partial t}, \quad \eta = \frac{k}{\phi C_t \mu} \tag{5}$$

where $C_t = C_r + C_f$ (Pa^{-1}) is the total value of rock compressibility (C_r) and reservoir fluid compressibility (C_f), and t (s) is the elapsed time from the start of CO_2 injection. The hydraulic diffusivity, η, is a hydraulic parameter that controls the unsteady pressure transient.

The pressure build-up in an injection well, defined as p_i, under the general steady-state radial flow is proportional to the fluid injection rate q (m^3/s), while it is inversely proportional to the transmissivity (or permeability-thickness product) $K = kH$ (m^3), which is product of the horizontal permeability k and the reservoir thickness H (m) (Dietz, 1965). The transmissivity K expresses the flow capacity and ability in aquifers and reservoirs. The radial flow solution for the steady-state ($\partial p/\partial t = 0$) in Eq. (6) is given by the following equation (Van Everdingen and Hurst, 1949; IEAGHG, 2010):

$$p_i = \frac{\mu q}{2\pi k H} \ln\left(\frac{r_e}{r_w}\right) \tag{6}$$

where r_e (m) is the effective reservoir radius, which is the extent from the injection well to the reservoir boundary where the pressure is equal to the initial hydrostatic pressure; and r_w (m) is the injection well radius.

Assuming that the reservoir fluid is uniform and uncompressible ($C_f = 0$ and $\rho = $ const.), a typical solution of radial transient flow can be expressed as (Goode and Thambynayagam, 1987):

$$p(r,t) - p_0 = \frac{\mu q}{4\pi H k}\left(\ln\frac{kt}{\phi \mu C_t r^2} + 0.809\right) \tag{7}$$

where p_0 is the initial or outer boundary pressure of the aquifer, and $\mu q/(4\pi kH)$ is a constant for a constant if the injection rate q is set as a constant without considering skin factors. This solution shows the reservoir pressure build-up at different injection periods and different radial distances from the injection well. The transient pressure changes in the aquifer at the elapsed time from the start of injection are expressed by the transient flow equation and are shown in Fig. 4.

The pressure response at the observation well at $r = r_m$, Δp (Pa), can be estimated by

$$\Delta p(t) = p(r_m, t) - p_0 \tag{8}$$

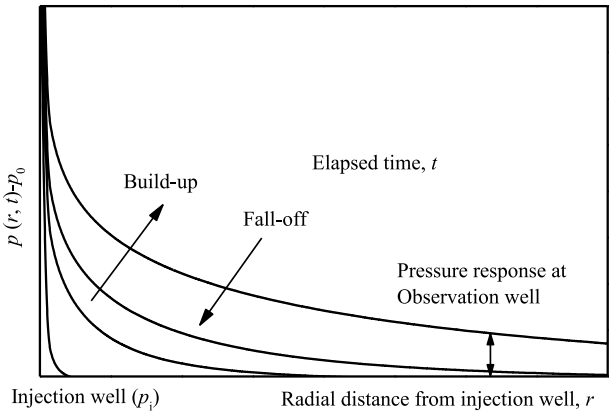

Fig. 4. Schematic solution showing transient pressure for pressure build-up at an injection well.

The pressure calculated by Eq. (8) is roughly equal to the pressure changes between build-up and fall-off at $r = r_m$. The transient condition is applicable only if the pressure response in the aquifer is assumed to be not affected by the presence of the outer boundary; thus, the reservoir appears infinite in extent. In this study, a constant pressure boundary was assumed to be close to an aquifer with enough radius. Therefore, it is possible to use this equation to estimate the rough pressure response at the observation well.

The distance from the CO_2 injection well to the observation well ($r = r_m$) is the critical parameter that controls the magnitude of the pressure response at the observation well, which is affected by the CO_2 injection rate and amount from the injection well and the aquifer parameters. According to Eq. (7), the magnitude of the response pressure is directly proportional to the injection rate, q, and injection period, while the transmission delay time is inversely proportional to the hydraulic diffusivity of the aquifer. The pressure response is almost inversely proportional to distance r_m.

3.2. Analysis method

The initial pressure of the aquifer was set as $p_0 = 10$ MPa in the present simulations. The BHP in the injection well is equal to $p_0 + p_i$. The pressure response and distribution of CO_2 saturation in the aquifer were simulated for a constant CO_2 mass injection rate q_m (t-CO_2/d) as shown in Fig. 5.

When the injection well is shut-in after the CO_2 injection for a period, t_i, the pressure response of the observation well changes and has a peak value Δp_{max}, which is recorded after the delay time, Δt_{max} from the shut-in of the injection well. A pressure response

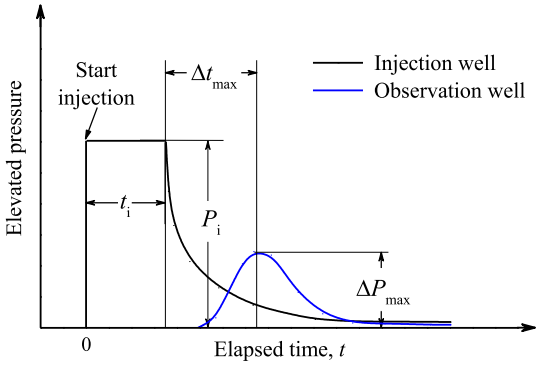

Fig. 5. Schematic diagram of defined variables.

Δp_{max} is sensitive to the magnitude of pressure build-up p_i. Therefore, it is expected that the ratio of both pressures defined as

$$R = \frac{\Delta p_{max}}{p_i} \tag{9}$$

is not sensitive to injection rate q. Simulations were carried out to investigate the pressure response and the delay time of the peak pressure in the observation well by comparing the CO_2 plume front position extending outward. In the present simulations, the CO_2 injection rate q was controlled according to the BHP, which must be less than the threshold capillary pressure and sufficiently less than the fracture pressure of the caprock or upper sealing layer. The maximum BHP has been set as 90% of the threshold capillary pressure (12.6 MPa = 14 MPa × 0.9) measured for the Moebetsu Formation (Osiptsov, 2017). In the base model, the CO_2 mass injection rate was set as q_m = 600 t-CO_2/d (q = 3.744 m^3-std/s, ρ_{CO2} = 1.855 kg/m^3 at the surface condition). The injection period in the base model was assumed to be t_i = 100 d, and the distributions of the pressure response and CO_2 saturation were simulated until t = 1000 d from the start of CO_2 injection.

4. Pressure build-up at the injection well and pressure response at the observation well

4.1. Effect of perforation scheme for injecting CO_2

The CO_2 injection well was assumed to be a vertical well. As different perforation schemes will lead to a difference in pressure build-up at the well, the effects of the perforation scheme on the CO_2 injectivity were discussed. As shown in Fig. 6, some previous studies used different simulation models with several perforation points and locations for CO_2 injection (Cinar et al., 2008; Chadwick et al., 2009). In this study, the multiple perforation scheme using 10 holes perforated in the center of each layer (Fig. 6a) was used. Chadwick et al. (2009) used the scheme with an injection point located 10 m below the aquifer ceiling (Fig. 6b) to study the pressure build-up at the injection well and pressure distribution in the aquifer. Cinar et al. (2008) used the scheme with the injection point located in the middle of the reservoir (Fig. 6c).

Fig. 7 shows the pressure build-up at the injection well with different perforation schemes for CO_2 injection using the same injection rate. It can be seen that the injection with one perforation point will lead to a significant pressure build-up in the first hour of injection, which is more than twice that of all the perforations (Fig. 6a). In the multiple perforation scheme, a larger contact area with the reservoir results in a smaller pressure build-up and less stress on the sealing layer for the same injection rate. Furthermore,

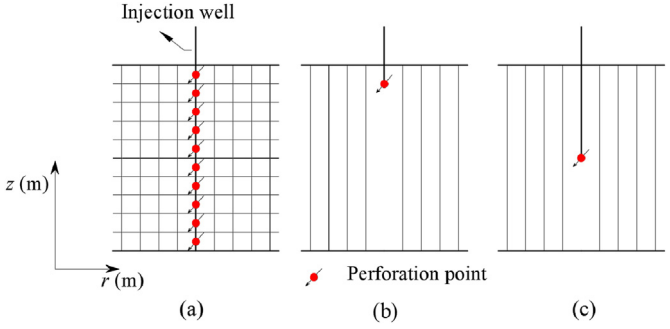

Fig. 6. Injection well perforation schemes used in previous studies: (a) Multiple perforations, (b) Single perforation hole at the top used by Chadwick et al. (2009), and (c) Single perforation hole at a position used by Cinar et al. (2008).

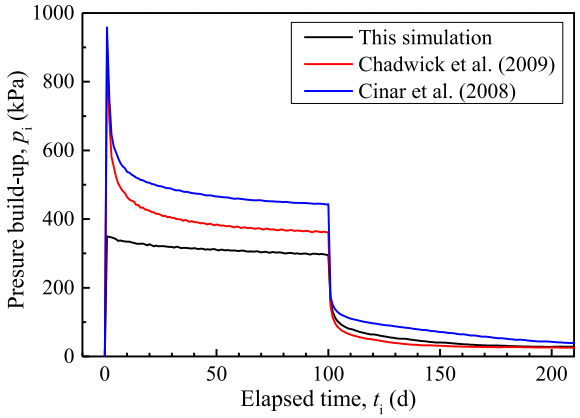

Fig. 7. Numerical simulation results on pressure build-up of the injection well obtained with different perforation methods of the CO_2 injection well using CMG-STARS™.

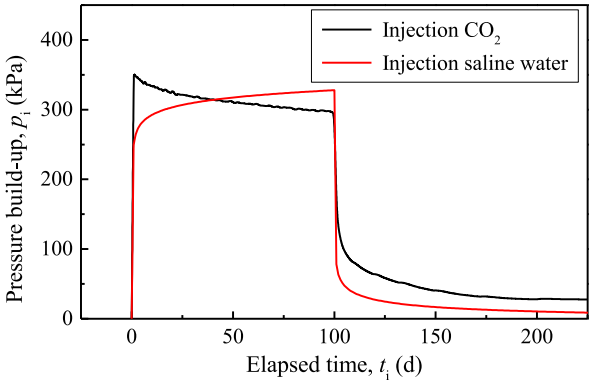

Fig. 8. Pressure build-up by injecting CO_2 and saline water vs. elapsed time for the base model.

only one block in the vertical direction may not be rigorous to study the pressure build-up. If the pressure gradient of the reservoir is not considered, the calculated BHP may be overestimated. Therefore, in this study, a multiple perforation scheme was used in the simulations to ensure a safe injection with a smaller pressure build-up at the well.

4.2. Pressure build-up and bottom-hole pressure

To study the pressure build-up at the CO_2 injection well, an injection scheme based on the base model for injection rate q_m = 600 t-CO_2/d and continuous injection for 100 d (t_i = 100 d) was simulated compared with the case of injecting saline water that is the same with the reservoir fluid. Injecting CO_2 and saline water will show the same volume flow rates in the reservoir condition.

After the start of injecting CO_2 into the aquifer, CO_2 saturation around the injection well increased with replacing saline water. Therefore, with increasing CO_2 saturation, the viscosity μ of the aquifer fluid, especially around the injection well, gradually changed from the viscosity of saline-water ($\mu_{brine} \approx 6 \times 10^{-10}$ Pa s) to that of supercritical-CO_2 viscosity ($\mu_{CO2} \approx 0.429 \times 10^{-10}$ Pa s). As shown in Fig. 8, a decrease in the transient pressure after a pressure build-up of 350 kPa was observed during CO_2 injection at a constant injection rate, while the pressure build-up during saline water injection gradually increased. However, at the early stage of CO_2 geological storage, the magnitude of pressure build-up (≈350 kPa)

is similar even if different fluids are injected, because the CO_2 storage area is limited around the well. Moreover, CO_2 saturation is also limited to less than 35%, based on the relative permeability curves shown in Fig. 3, when CO_2 dissolution into saline water is neglected. Therefore, the pressure change ($\approx$50 kPa) during the CO_2 injection period (100 d) is not proportional to the fluid viscosity, even if the viscosity of CO_2 is less than 10% of the viscosity of saline water. Thus, using the viscosity of saline water in Eq. (6) instead of that of CO_2 shows a more realistic estimation of the pressure build-up in the aquifer at the initial injection stage. However, the pressure build-up estimated by Eq. (6) using the viscosity of saline water is slightly overestimated than that of CO_2. This difference can also be explained by the equation presented by Cinar et al. (2008) and IEAGHG (2010). They modified Eq. (6) by introducing the relative permeability of CO_2. However, introducing CO_2 relative permeability is another complicated question as CO_2 relative permeability changes with continuous injection, adding more uncertain variables. In this study, the viscosity of saline water is used to estimate the rough pressure build-up using Eq. (6).

In the present simulations, the radial flow consisting of saline water and CO_2 was calculated considering the relative permeability curves for each fraction. Therefore, physical property changes in the blocks including multi-phase flow were simulated automatically in the present simulations using CMG-STARS™.

Fig. 9 shows the cross-sectional simulation results for the r and z axes of CO_2 saturation and CO_2 plume flux vectors at t = 10, 50, 100 and 200 d after the start of CO_2 injection. The CO_2 plume expands mainly as a radial flow, because the horizontal permeability, k, or hydraulic diffusivity, η, is 10 times larger than that of the vertical value. The buoyancy force on unit CO_2 volume (roughly 4000 kN/m^3) induces vertical CO_2 convection flow, because of the density

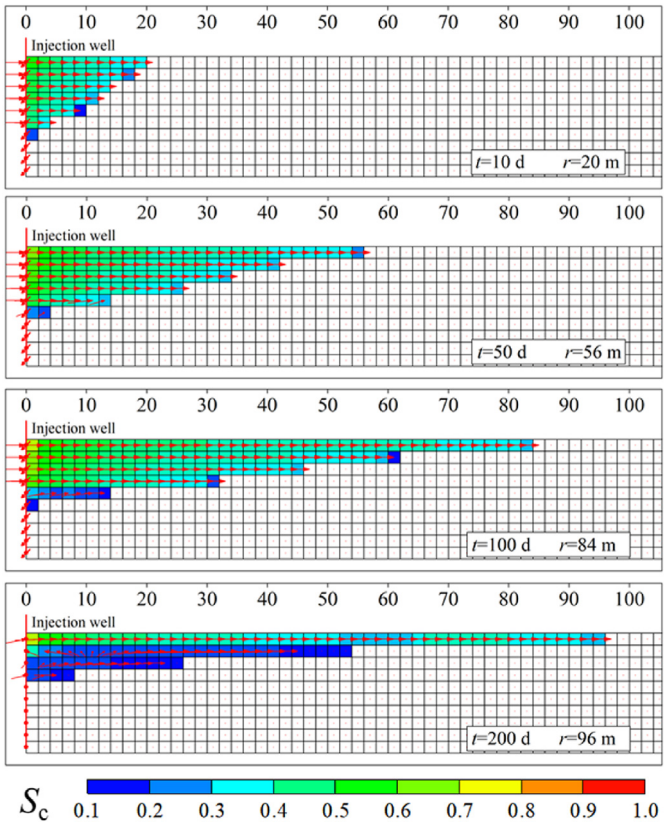

Fig. 9. Cross-sectional on r and z axes of CO_2 saturation and CO_2 plume flux vectors at t = 10, 50, 100 and 200 d for the base model.

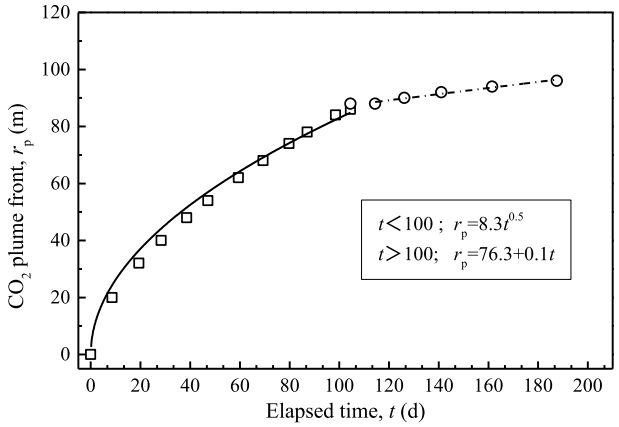

Fig. 10. CO_2 saturation front distribution over time.

difference between injected supercritical CO_2 ($\approx$600 kg/m^3) and saline water (=1030 kg/m^3) in the aquifer. Therefore, the top layer of the aquifer shows the largest expanding CO_2 seepage flow velocity with the farthest CO_2 plume front. Most CO_2 fluids accumulate and trap between caprocks and reservoirs which is widely recognized as structure trapping. This phenomenon makes it easy to build up extremely pressure which will threaten the safety of caprock. The red arrows in Fig. 9 show the flow velocity vectors. It is clear that the CO_2 plume diffuses mainly in the radial direction during the CO_2 injection period, while the convection in the vertical direction is much slower. After the injection well was shut-in, the driving pressure in the horizontal direction gradually vanished with fall-off pressure, and the vertical buoyancy flow becomes prominent.

We defined the CO_2 plume front position at the top layer, r_p, where the CO_2 saturation is S_c = 10%. As shown in Fig. 10, the plume front is observed at r_p = 84 m on the 100th day. Fig. 10 shows the CO_2 plume front position, r_p, before and after stopping CO_2 injection at t = 100 d (= t_i). The CO_2 plume front position, r_p, expands almost proportionally to $t^{0.5}$ for 0< t < 100 d. After the injection well was shut-in at t > 100 d, the CO_2 front slowly expands proportionally to 0.1t by buoyancy force on the CO_2 plume.

The numerical simulation results of the base model for the distributions of the reservoir pressure change from the initial aquifer pressure ($p(r)-p_0$) and CO_2 saturation ($S_c(r)$) at t = 50 and 100 d are shown in Fig. 11.

It can be seen that pressure changes and CO_2 saturation distributions are correlated in the region of CO_2 saturation S_c > 35%, while only a pressure change is observed in the region (r > 100 m) with a CO_2 saturation $S_c \approx 0$. Assuming the position of the CO_2 plume front defined by S_c = 10%, the pressure transmitting speed is two orders of magnitude higher than that of the CO_2 plume front, because the pressure change is observed without CO_2 saturation change.

4.3. Effect of CO_2 injection rate and aquifer transmissivity on pressure build-up

Fig. 12 shows the simulation results of pressure build-up, p_i at the CO_2 injection well for injection rate, q_m, compared with the estimated line calculated using Eq. (6) by assuming the viscosity of saline water, as discussed in the previous section. The pressure build-up does not show a significant linear relationship with injection rate. As discussed previously, this can be explained by the changing CO_2 saturation around the injection well, since the relative permeability changes with CO_2 saturation. The simulation

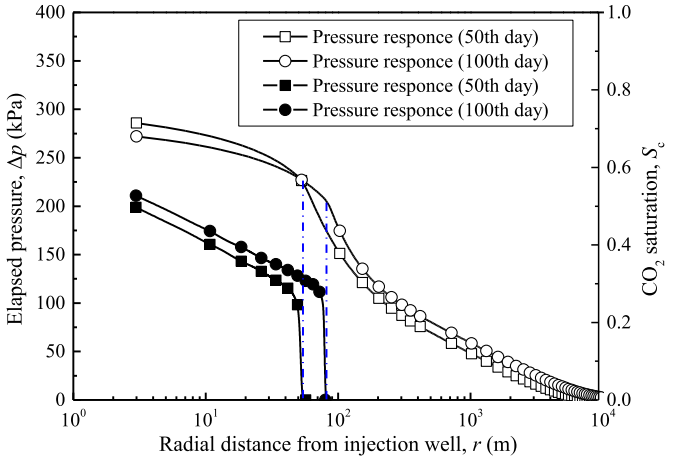

Fig. 11. Numerical simulation results of pressure response vs. CO_2 saturation at different distances from the injection well.

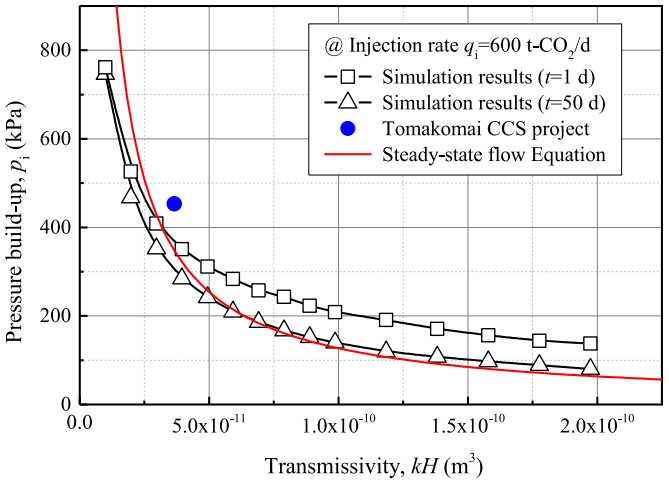

Fig. 13. Pressure build-up, p_i (kPa) vs. aquifer transmissivity, kH (m^3).

results show that the linearity between p_i and q_m is better and closer to the values estimated by Eq. (6) with a low injection rate $q_m < 600$ t-CO_2/d than that with a large injection rate $q_m > 1500$ t-CO_2/d. This is because the higher injection rate results in a faster change in CO_2 saturation around the injection well.

We confirmed that the pressure build-up can be correctly estimated using saline water viscosity to be 65% because the CO_2 saturation around the injection well is close to 35%. This setting will be used to calculate the pressure change in the reservoir below.

CO_2 injection into the Moebetsu Formation was conducted and the maximum pressure build-up of the injection well (IW-2) was recorded around $p_i = 450$ MPa at the injection rate $q_m = 600$ t-CO_2/d and injection time $t_i = 50$ d. The thickness of the Moebetsu Formation is approximately 100–200 m which is uncertain and different from the base model set. Simulations were run, and the pressure build-up against different transmissivities of the aquifer was studied. According to the simulation results shown in Fig. 11, the transmissivity of the Moebetsu Formation is approximately $K = 2.7 \times 10^{-11}$ m^3, and the permeability of the Moebetsu Formation was calculated as 135×10^{-15}–270×10^{-15} m^2, which is different from our base model setting $k = 363 \times 10^{-15}$ m^2 that is overestimated according to a comparison between the field pressure data and simulation results. Owing to the short injection period, the fluid flow around the injection well is in an unsteady state. In Fig. 13, the pressure build-up at the injection well after $t = 1$ and 50 d, with respect to aquifer transmissivity K, were compared with those in the steady-state flow (Eq. (6)). As at the early stage of injection, there is a transient effect of pressure build-up at the injection well, and the pressure build-up of the injection well on the 50th d is closer to the steady-state flow than with that on the 1st d. A higher transmissivity aquifer is becoming closer to the calculated pressure build-up, p_i of steady-state flow.

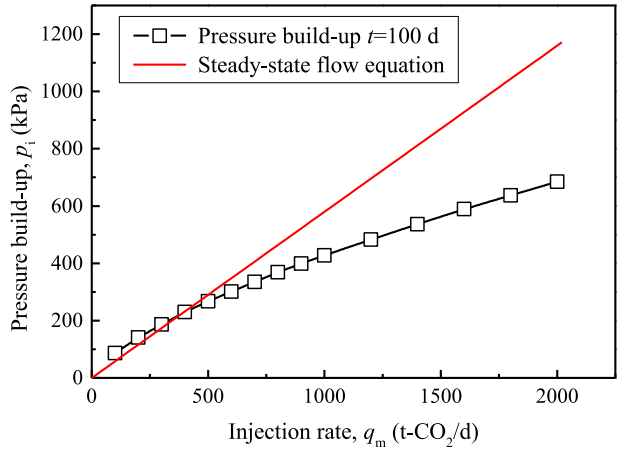

Fig. 12. Numerical simulation results of pressure build-up p_i vs. CO_2 mass injection rate q_m.

4.4. Pressure fall-off at the CO_2 injection well

Opening or shutting off a well causes pressure changes in the CO_2 injection well. The CCS projects including fall-off data after shut-in can be used to study the aquifer state (Escobar and Montealegre, 2008). When the BHP vs. time plots are measured with sufficient precision after the well shut-in, the aquifer in situ permeability and well skin factor can be estimated by analyzing the data. This is similar to the well-testing method widely used in petroleum reservoir engineering. Without considering the skin factor, the pressure fall-off function in the injection well is expressed by the radial transient flow equation (Eq. (7)). The pressure p_0 should be modified to the instantaneous BHP when the injection well is shut in. Because $q\mu/(4\pi kH)$ can be treated as a constant if the injection rate q is constant, the hydraulic diffusivity η can be considered the main parameter controlling the fall-off curve.

In contrast to the conventional method of analyzing pressure fall-off lines, the pressure fall-off time is defined in this study to

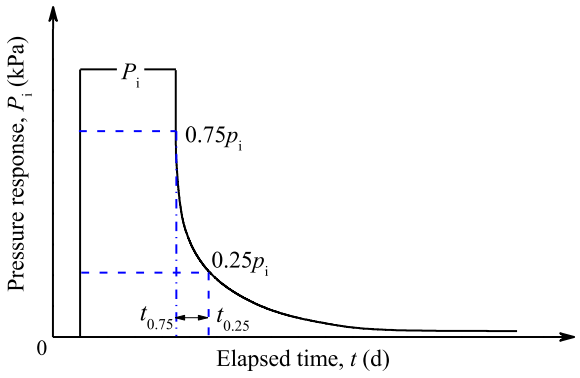

Fig. 14. Definition of pressure fall-off time after pressure build-up.

analyze reservoir conditions and pressure transients. As shown in Fig. 14, $t_{0.75}$ and $t_{0.25}$ are defined as the elapsed times to reach 75% and 25% pressure reductions from the build-up pressure after the well shut-in. The pressure fall-off time is defined as ($t_{0.75}$−$t_{0.25}$), which shows the period the pressure falls off 50% of the built-up pressure.

In the case of CO_2 injection in the Moebetsu Formation, Tomakomai CCS project, some pressure fall-off data were recorded after shutting the well, and the fall-off time ($t_{0.75}$−$t_{0.25}$) was analyzed at about 5 d based on the BHP data. The numerical simulation results for the fall-off time ($t_{0.75}$−$t_{0.25}$) vs. hydraulic diffusivity η for the base model are shown in Fig. 15, which includes the results of different porosities (0.1, 0.2 and 0.3) and permeabilities k (= 98×10^{-15}–1960×10^{-15} m^2). As the fall-off time for the Moebetsu Formation (dotted line in Fig. 15) was 5 d, the hydraulic diffusivity range of the Moebetsu Formation can be estimated as $\eta = 2$–4 m^2/s from the simulation results of ($t_{0.75}$−$t_{0.25}$) and hydraulic diffusivity. As the transmissivity of the Moebetsu Formation was matched as $K = 2.7 \times 10^{-11}$ m^3 in the last section, and the thickness is between H = 100–200 m, porosity φ = 0.2–0.4. Therefore, the matrix rock compressibility of the Moebetsu Formation is estimated as $C_r = 0.14 \times 10^{-9}$–$1.11 \times 10^{-9}$ Pa^{-1}. This means that the rock compressibility set as $C_r = 0.9 \times 10^{-9}$ Pa^{-1} is within the reasonable range compared with the Moebetsu Formation.

4.5. Pressure response at observation wells

In this section, the pressure responses at a hypothetical observation well located at a range of radial distance r_m = 1000–5000 m from the injection well are discussed based on the simulation results by comparing the values estimated using Eq. (8). The maximum value of pressure response is defined as Δp_{max}, which is recorded at the observation well ($r = r_m$) after continuous CO_2 injection for t_i = 100 d in each injection scheme. Fig. 16 shows the numerical simulation results of the pressure response at the observation well located at r_m = 1000, 3000 and 5000 m against the CO_2 injection q_m = 600 t-CO_2/d for t_i = 100 d (base model). The pressure of the observation well increases gradually during the injection period, which is different from the pressure build-up of the injection well. This is because the pressure build-up in the vicinity of the injection well (less than r = 100 m) is influenced by both CO_2 and saline water flows, while the pressure disturbance around the observation well far from the injection well is not

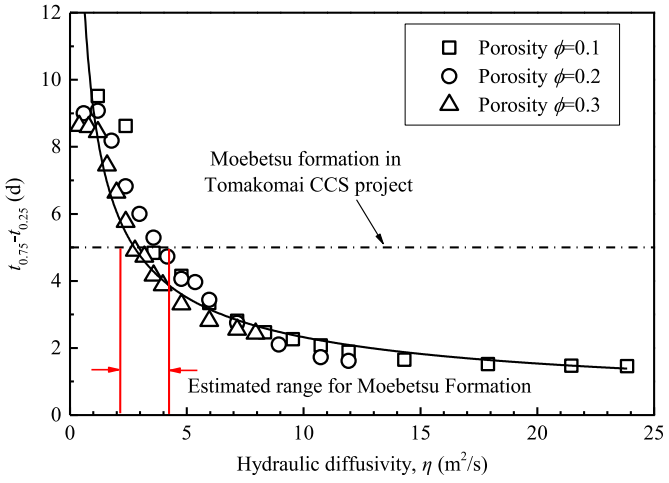

Fig. 15. Numerical simulation results of fall-off time ($t_{0.75}$−$t_{0.25}$) vs. hydraulic diffusivity η compared with the fall-off time of the Moebetsu Formation (5 d).

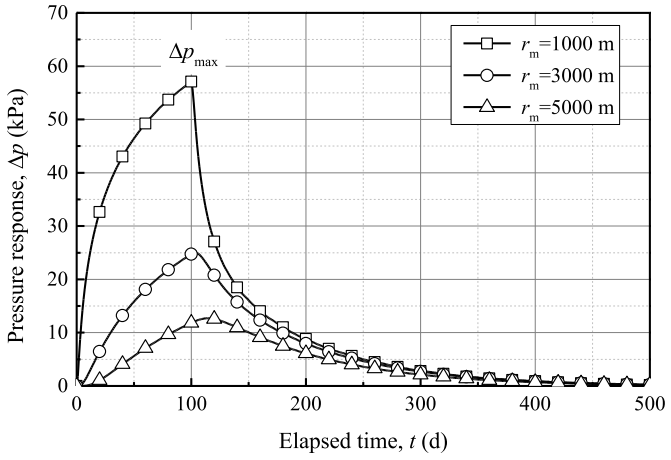

Fig. 16. Typical simulation results of the pressure response at the observation wells located at r_m = 1000, 3000 and 5000 m.

influenced by the difference in viscosities of CO_2 and saline water. After the injection well is shut-in ($t > t_i$), the observation well pressure draws a curve similar to the pressure fall-off of the injection well. It can also be seen that there is a time delay between the injection well shut-in to the peak pressure response of the observation well, and this delay time becomes larger as the distance from the injection well increases. The peak value of the pressure response, Δp_{max} becomes smaller and broader, and the peak time recorded at the observation well, Δt_{max}, increases with increasing distance from the injection well, r_m. For example, Δp_{max} = 57 kPa at r_m = 1000 m becomes more than twice (Δp_{max} = 25 kPa) at r_m = 3000 m.

As shown in Fig. 17, the simulation results of Δp_{max} have a linear relationship with the CO_2 mass injection rate q_m and are consistent with the numerical simulation results for injecting saline water. The analytical equation assuming a transient radial flow is expressed as

$$\Delta p_{max} = p(r_m, t_{max}) - p_0 \tag{10}$$

The analytical solution obtained with Eq. (10) is less than the simulation results. The difference between the results increases as the radial distance between the injection well and observation wells increases, because the value estimated by Eq. (10) can only be applied for a rough estimation. In this simulation study, the injection period was assumed to be t_i = 100 d, and the peak pressure response at the observation well can be detected after dozens of days.

5. Pressure ratio of injection well and observation well

5.1. Single CO_2 injection with pressure build-up and fall-off

To avoid the error in the absolute magnitude of the pressure response at the observation well, we introduced the parameter R, which is the ratio of the pressure build-up p_i and the maximum value of pressure response Δp_{max}. Both the pressure build-up at the injection well and the pressure response at the observation wells have almost linear relationships with the injection rate, q_m < 600 t-CO_2/d. This ratio can be used for determining the pressure response at the observation wells based on the pressure build-up, because the ratio $R = \Delta p_{max}/p_i$ is not sensitive to the mass injection rate, q_m. In addition, the term $q\mu_w/(4\pi kH)$ in Eq. (7) can be treated as a constant if the mass injection rate q_m is a constant. Therefore, the value of R is proportional to the injection period and hydraulic diffusivity but inversely proportional to the square of the radial

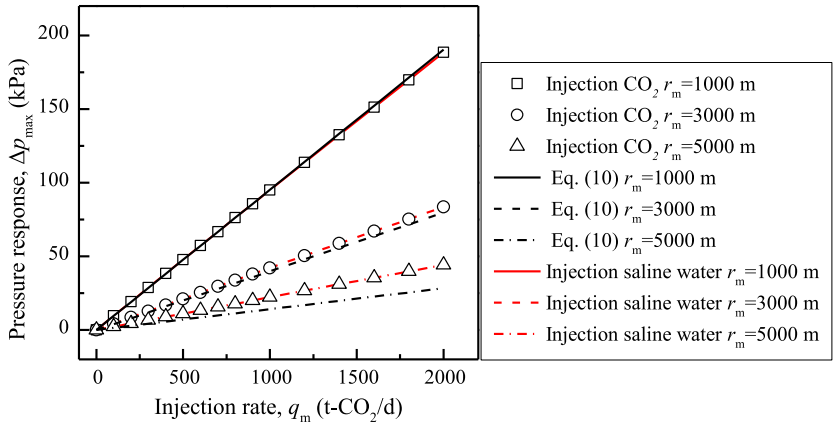

Fig. 17. Numerical simulation results of the pressure response at the observation wells vs. CO_2 mass injection rate q_m.

distance from the well, while it is not as sensitive to the CO_2 mass injection rate q_m. The rough value of R can be estimated by the following equation where hydraulic diffusivity, η, is defined by Eq. (5).

$$R = \frac{1}{2\ln(r_e/r_w)}\left(\ln\eta\frac{t_i}{{r_m}^2}+0.809\right) = 0.0434\left(\ln\eta\frac{t_i}{{r_m}^2}+0.809\right) \quad (11)$$

where C_t is equal to rock compressibility because fluid is assumed to be incompressible ($C_f = 0$), r_e = 10,000 m is the effective reservoir radius, and r_w = 0.1 m is the radius of the injection well. Eq. (11) shows that R consists of a logarithmic function of time t, aquifer area up to the inner area of the observation well radius (πr_m^2), and hydraulic diffusivity, η. Assuming that the observation well response to the peak pressure value occurs at the moment the injection well is shut-in, the time t in Eq. (11) is replaced with t_i.

The numerical simulations of R using CMG-STARS™ were performed for the base model with the horizontal permeability range from $k = 196 \times 10^{-15}$–784×10^{-15} m^2 (= 200–800 mD), the observation well location r_m = 1000–5000 m, and different injection periods t_i = 50–300 d; the porosity and compressibility of the porous media were considered constant (ϕ = 0.3 and $C_t = 1.4 \times 10^{-9}$ Pa^{-1}). A sensitive study of hydraulic diffusivity η was also carried out by setting the constant injection rate q_m = 600 t-CO_2/d. The simulation results of R compared with values calculated by Eq. (11) are shown in Fig. 18. It can be seen that the pressure ratio R shows an almost logarithmic function of $\eta t/r_m^2$. However, there is a slight difference between the values of R for different permeabilities, especially when $\eta t/r_m^2 > 10$. Because there is a time delay between the injection well shut-in and the observation well response to the peak pressure value, the time t of the simulation results shown in Fig. 18 was considered as $t = t_i + \Delta t_{max}$. Δt_{max} is defined as the time delay from the shut-in time at the injection well to the time when the observation well attains the peak pressure (Fig. 5). Thus, the pressure response at the observation well calculated by Eq. (11) is underestimated compared with the numerical simulation; however, both plots of R vs. $\eta t/r_m^2$ have a similar relationship expressed by the logarithmic function. It can also be seen that Eq. (11) is more suitable for a high-permeability aquifer as an aquifer with a larger permeability has a shorter time delay, and the simulation results of R will be closer to the value calculated by Eq. (11). This logarithmic function can help us deduce an evolution of the pressure at the observation well at different distances r_m, at different times according to the injection well pressure build-up of field data. The hydraulic diffusivity η was evaluated by the pressure fall-off lines after the shut-in. Therefore, the observation well location can be designed at an appropriate location, and a pressure transmitter with suitable pressure resolution can be selected for pressure monitoring.

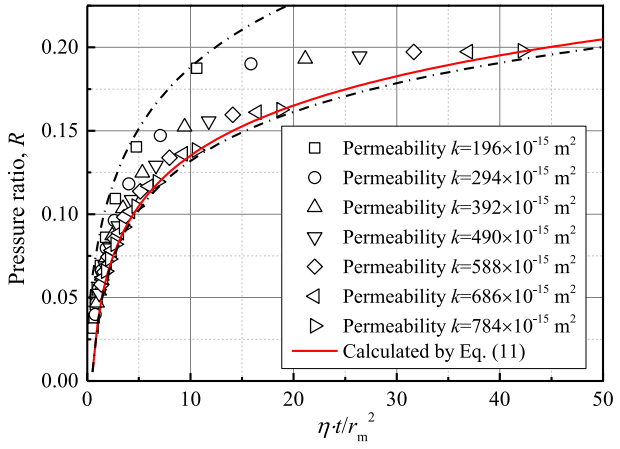

Fig. 18. Numerical simulation results of pressure ratio R for different permeabilities (q = 600 t-CO_2/d, t_i = 100 d, $k = 196 \times 10^{-15}$–784×10^{-15} m^2).

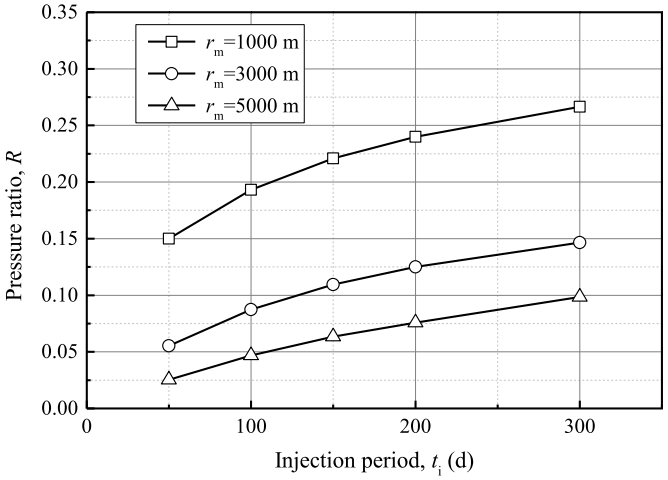

Fig. 19. Effect of injection period, t_i, on pressure ratio, R.

An empirical equation based on the simulation results in Fig. 18 was summarized without considering the time delay Δt_{max}, and it is given by

$$R = \frac{\Delta p_{max}}{p_i} = (0.0425 - 0.06)\left(\ln \eta \frac{t_i}{r_m{}^2} + 0.809\right) \quad (12)$$

The pressure ratio at an observation will have a large variation at different permeability aquifer conditions. Eq. (12) can be applied to the Tomakomai CCS project, and it can also be applied to other CCS projects with the pressure ratio $\eta t/r_m^2 < 10$. In addition, a specific analysis of the pressure ratios against different variables can be performed to make a relatively more accurate assessment for a planned CCS project in the future.

According to the simulation results of pressure build-up at the CO_2 injection well and pressure response at the observation well, it is expected that the pressure ratio R increases with increasing injection period because the pressure build-up at the injection well p_i decreases with increasing CO_2 injection period t_i. In contrast, the response pressure at the observation well Δp_{max} becomes higher. Fig. 19 shows the numerical simulation results of the pressure ratio R for different injection periods from t_i = 50–300 d. The higher response pressure can be monitored by increasing the injection period because R increases with t_i.

The pressure ratios at different distances from the injection well for the base model ($k = 363 \times 10^{-15}$ m^2) compared with the pressure ratio in an aquifer with permeability $k = 196 \times 10^{-15}$ and 784×10^{-15} m^2 (= 200 and 800 mD) are shown in Fig. 20. The pressure fluctuates with the permeability of the aquifer. As shown in Fig. 18, there is a small difference between the values of R for different permeabilities, especially when $\eta t/r_m^2 > 10$. Fig. 20 more intuitively reflects the pressure ratio change with the increasing radial distance from the injection well. The pressure ratio, R, changes faster when the radial distance from the injection well is smaller. However, as the upper limit pressure response at the observation well is small, it is easy to estimate the pressure for choosing an effective pressure sensor. In the Tomakomai CCS project, the observation well OB-2 was drilled at $r_m \approx 3000$ m from the injection well to monitor the pressure change caused by CO_2 injection. The present simulation result for q_m = 600 t-CO_2/d and t_i = 100 d shows that R = 0.09 at r_m = 3000 m.

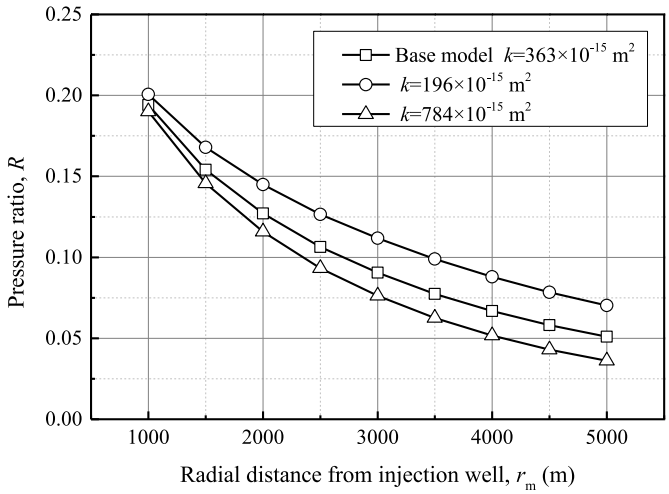

Fig. 20. Pressure ratio vs. radial distance from the injection well (t_i = 100 d) for the base model.

5.2. A case of multiple CO_2 injections

For the Tomakomai CCS project, the CO_2 injection pattern at the early stage of the project comprised a series of injections with multiple pressure build-ups and fall-offs. The CO_2 injection status was tested to check the pressure build-up against the injection rate at the early stage of CO_2 injection. A model case used to investigate the pressure response by multiple CO_2 injections is shown in Fig. 21. The multiple injection model includes six cycles with t_i = 100 d as injection period and t_s = 30 d as shut-in period based on the Tomakomai CCS project (Singh, 2018). The parameters used in the numerical simulation were the same as those for the single injection model (Table 1).

The simulation results of pressure build-up at the injection well and pressure response at the observation well are shown in Fig. 22. The pressure responses of the observation wells located 3000 m away from the injection well are shown in Fig. 22. The first CO_2 injection cycle is the same as the single injection case (base case) until the second cycle starts. It can be seen that each injection causes a pressure response peak at the observation well and draws down in the injection well, similar to the pressure fall-off in the case of single build-up and fall-off. The BHP in the injection well shows a slight drop due to the changing CO_2 saturation and fluid viscosity around the injection well as discussed for the single build-up and fall-off case. The pressure build-up in each injection decreases, while the pressure response Δp_{max} in each corresponding injection at the observation well gradually increases.

The reservoir flow around the injection well turns to a steady state after injecting a large amount of CO_2 into the reservoir in a single cycle. As shown in Fig. 22, the case of multiple CO_2 injections shows a broader pressure response. Fig. 23 shows the pressure response at the observation wells and the pressure ratio for the distance r_m = 3000 m from the injection well. The peak pressure value at the observation well turns to be a stable value, which is similar to the pressure build-up at an injection well. Thus, the pressure ratio also approaches to a stable value. This is more convenient for determining a reliable pressure ratio in the simulation study.

5.3. Delay time of the pressure response at the observation well

Even if the injection well is shut-in and returns to the initial pressure, the pressure transmitted in the aquifer continues moving outward with depleting its amplitude. Fig. 24 shows the numerical simulation results of time delay Δt_{max} in the aquifer with the horizontal permeability range from $k = 196 \times 10^{-15}$–784×10^{-15} m^2 (=

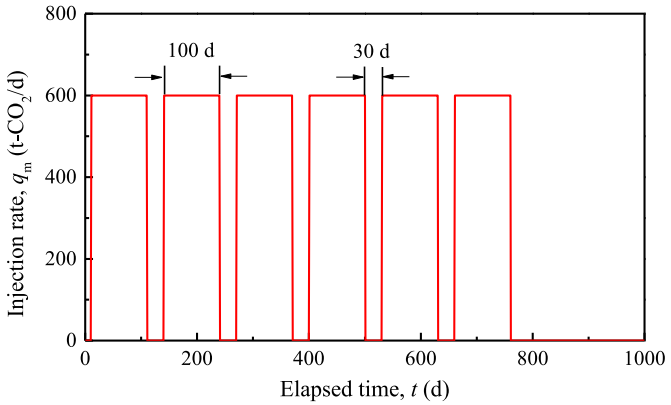

Fig. 21. A model case of CO_2 multiple injections consists of six injection cycles with t_i = 100 d as injection period and t_s = 30 d as shut-in period.

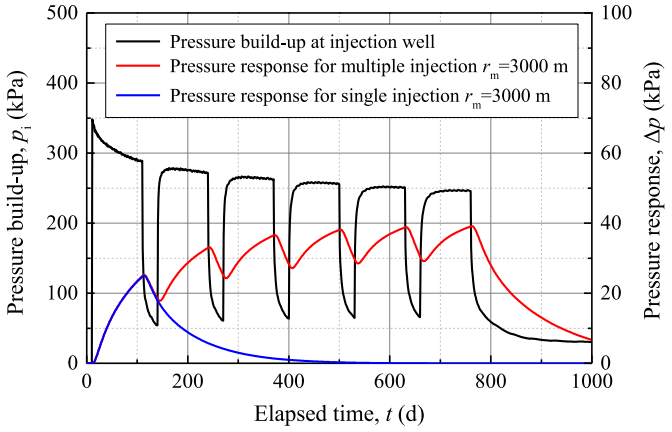

Fig. 22. Pressure build-up of the injection well and pressure response in multiple-injection and single injection cases for the observation well at r_m = 3000 m.

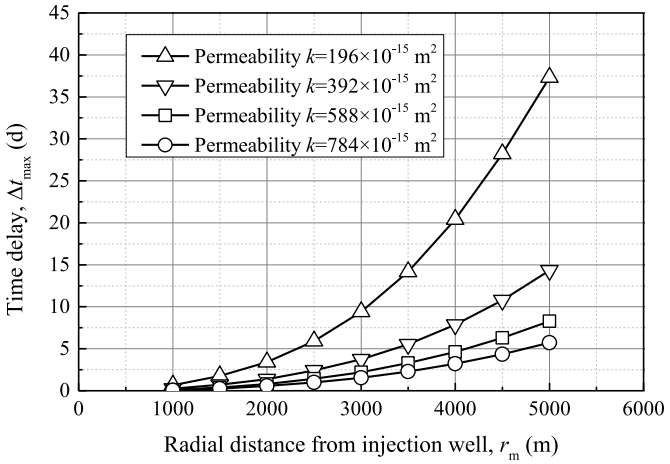

Fig. 24. Numerical simulation results of time delay Δt_{max} of the pressure response peak for the observation wells located at the radial distance r_m (base model, injection period t_i = 100 d).

200–800 mD) at the observation wells with different radial distances (r_m = 1000–5000 m) from the injection well. As discussed above, fluid flow transmits faster in a high-permeability aquifer, and the pressure transmitting speed is two orders of magnitude higher than that of the CO_2 plume. The time delay Δt_{max} is proportional to the distance from the injection well and inversely proportional to the aquifer permeability. The time delay Δt_{max} increases exponentially with increasing radial distance r_m. For example, the time delay value for an observation well located at the radial distance r_m = 1000 m occurs the peak pressure value on the day of shut-in of the injection well, while it takes about t = 37 d to detect a peak pressure response from an observation well located at a radial distance r_m = 5000 m for a reservoir with permeability $k = 196 \times 10^{-15}$ m^2.

The pressure response at the observation well shows a pressure peak that is almost proportional to the pressure build-up at the injection well. The delay time, Δt_{max}, as defined in Fig. 5, was found to be the peak value on the curve of $p(r_m)$ vs. t for r_m = 1000–5000 m and permeability $k = 196 \times 10^{-15}$–784×10^{-15} (= 200–800 mD).

The simulation results of Δt_{max} vs. r_m^2/η are summarized in Fig. 25. It can be seen that the time delay Δt_{max} is almost linearly proportional to r_m^2/η, which is inversely proportional to the

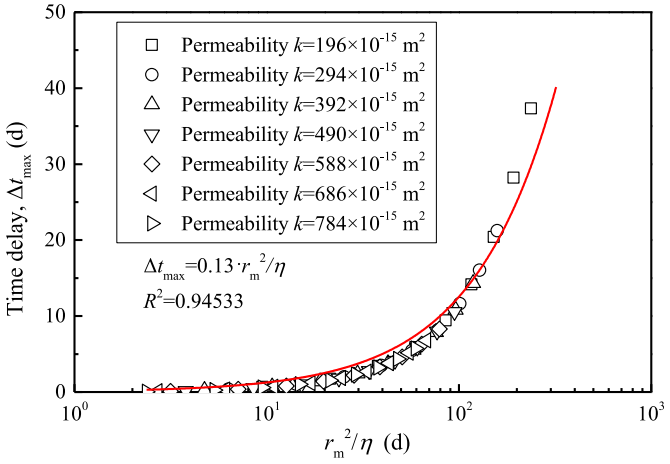

Fig. 25. Time delay of the observation wells with r_m = 1000–5000 m for different permeabilities.

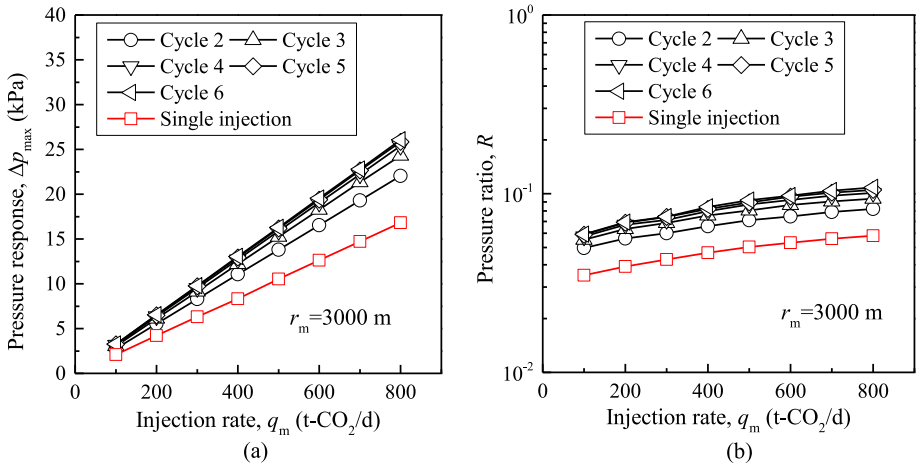

Fig. 23. Pressure response and pressure ratio R in the observation well at r_m = 3000 m for the multiple-injections model compared with the single injection model (base case) vs. injection rate q_m: (a) Pressure response, and (b) Pressure ratio R.

horizontal permeability, k. The relationship can be summarized as follows:

$$\Delta t_{\max} = 0.13\frac{r_m^2}{\eta} = 0.13\frac{\phi C_t r_m^2 \mu}{k} \quad (13)$$

The time delay $\Delta t_{\max}$ can be used as a reference parameter to assess the hydraulic transmission capacity of aquifers.

As discussed above, both the time delay $\Delta t_{\max}$ and the pressure fall-off time $(t_{0.75}-t_{0.25})$ can be used as important parameters to evaluate the hydraulic diffusivity η of an aquifer. Fig. 26 shows the numerical simulation results of the relationship between the hydraulic diffusivity η and time ratio $\Delta t_{\max}/(t_{0.75}-t_{0.25})$. Both time delay and fall-off time are inversely proportional to the hydraulic diffusivity, and the time ratio is inversely proportional to the hydraulic diffusivity. The approximate magnitude of the time ratio in different hydraulic diffusivity aquifers was estimated. It is convenient to estimate the time delay of peak pressure using the time ratio when the fall-off time is measured. For example, for $r_m = 3000$ m, $\Delta t_{\max}$ is equal to $(0.4–0.7)(t_{0.75}-t_{0.25})$ for $\eta = 2–4$ m^2/s corresponding to the range of the Tomakomai CCS project.

5.4. Design of observation wells for CO_2 geological storage

In this section, pressure responses at an observation well are analyzed to discuss the effect of the radial distance from the injection well ($r_m > 1000$ m) and the pressure sensor resolution installed in it.

Table 2 shows the simulation results of the pressure at the observation well range with different radial distances from the injection well. For example, in the case of the observation well, the distance is equal to $r_m = 3000$ m, the minimum sensitivity of the pressure transmitter needs approximately 1 kPa order under the absolute pressure (or pressure resistance) of 10–11 MPa to obtain an accuracy of two digits. However, in the case of the minimum sensitivity of 10 kPa order, the well distance required should be lesser than $r_m = 1000$ m.

The pressure build-up of the Tomakomai CCS project is about 450 kPa, and the observation well OB-2 is drilled with a distance $r_m = 3000$ m from the injection well. According to the calculation, the maximum pressure value might be $\Delta p_{\max} = 27$ and 35 kPa after $t = 50$ and 100 d injection, respectively. The specific resolution of the pressure transmitter installed in the observation well at $r_m = 3000$ m is required to be less than 1 kPa that is a tough specification under absolute pressures of 10–11 MPa to analyze aquifer permeability characteristics.

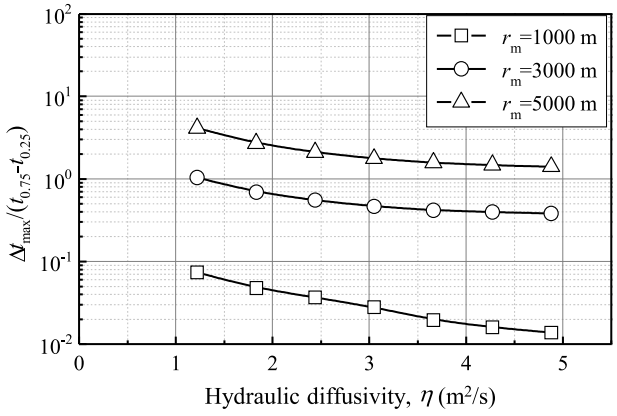

Fig. 26. Numerical simulation results of time ratio against hydraulic diffusivity η.

Table 2
Resolution required for pressure measurement at the observation wells ($r_m = 1000–5000$ m, $p_i = 1000$ kPa).

Radial distance, r_m (m)	$t_i = 50$ d		$t_i = 100$ d	
	Pressure response, $\Delta p_{\max}$ (kPa)	Specific resolution (kPa)	Pressure response, $\Delta p_{\max}$ (kPa)	Specific resolution (kPa)
1000	144–156	5	190–200	5
2000	73–100	5	116–145	5
3000	41–70	1	76–112	1
4000	25–51	1	52–88	1
5000	18–38	1	36–70	1

6. Conclusions

In this study, numerical simulations on pressure responses at injection and observation wells for CO_2 geological storage in a deep saline aquifer were done for CO_2 injection rate and aquifer characteristics, such as permeability or transmissibility and hydraulic diffusivity. The pressure responses and their time delay at the observation well become base data to check whether the aquifer model is enough reasonable to simulate the CO_2 storage. If the pressure measurement result at the observation well at the early stage of the CO_2 storage project matches the numerical prediction result using the aquifer simulation model, it can be one of the data proofing accuracies of the simulation model. Especially, the pressure ratio of the pressure response at the observation against a pressure build-up and fall-off at the injection well has been predicted as the judgment index of pressure change that is mainly related to the distance between injection and observation wells, but not sensitive to the injection rate. Therefore, it is essential to determine the location of the observation well and select a pressure transmitter with a reasonable resolution to measure the pressure response induced by the pressure build-up. The comparison of the simulation results and the actual measured results at the observation well provides whether the wide-area aquifer modeling used for the simulation is enough to correct or not. The results can be summarized as follows:

(1) The pressure build-up p_i is proportional to q/K, and gradually tends to be saturated and maintains a slight dropping rate with increasing CO_2 saturation around the injection well due to decreasing reservoir fluids viscosity. Eq. (6) for steady-state flow can be used for a rough estimation of the pressure build-up of the injection well by assuming saline water saturated in the aquifer.

(2) The numerical simulation results of pressure build-up, and fall-off at the injection well were analyzed by comparing the field data of the Tomakomai CCS project, the transmissivity of the Moebetsu Formation targeted in the project was estimated roughly as $K = 2.7 \times 10^{-11}$ m^3 and the hydraulic diffusivity of the reservoir is $\eta = 2–4$ m^2/s. Therefore, assuming that the permeability of the Moebetsu Formation is $k = 135 \times 10^{-15}–270 \times 10^{-15}$ m^2 and the porosity is $\varphi = 0.2–0.4$, and the rock matrix compressibility of the Moebetsu Formation is estimated as $C_r = 0.14 \times 10^{-9}–1.11 \times 10^{-9}$ Pa^{-1}.

(3) The radius of the CO_2 plume top front expands approximately proportionally to $t^{1/2}$ before $t < t_i = 100$ d, and after shut-in of the injection well at $t = t_i$, the top front is slowly expanding with proportionality to $0.1t$ due to buoyancy force on the CO_2 plume. The numerical simulation results on the pressure ratio R defined as the corresponding response pressure peak at the observation well ($\Delta p_{\max}$) overpressure build-up in the injection well (p_i) were analyzed, and a rough

estimation value of R at the observation well location ($r = r_m$) has been presented in Eq. (12).

(4) In the case of six cycles of CO_2 injections of 100 d injection and 30 d shut-in, R for each response pressure peak at the observation well shows an almost same value as that of the single injection case.

(5) The time of Δt_{max} from shut-in to the time observing the response pressure peak at the observation well is directly proportional to the radial distance from the injection well (r_m) and inversely proportional to the hydraulic diffusivity of the aquifer (η), but it is not sensitive to the injection rate (q).

(6) The peak value of pressure response at the observation well at a radial distance from the injection well of $r_m = 3000$ m was simulated as 27–35 kPa for the pressure build-up of 0.45 MPa at the injection well. The specific resolution of the pressure transmitter set in the observation well at $r_m = 3000$ m must be less than 1 kPa to obtain two or more valid digits.

Declaration of competing interest

The authors declare that they have no known competing financial interests or personal relationships that could have appeared to influence the work reported in this paper.

Acknowledgments

We acknowledge the funding support from the Research Fund for the special projects in key fields of Guangdong Universities (Grant No. 2021ZDZX4074), the Japan Society for the Promotion of Science (Grant No. JP-20K21163), and Scientific Research Fund of Hainan University (Approval No. KYQD(ZR)-22122).

References

Buscheck, T.A., Sun, Y., Chen, M., et al., 2012. Active CO_2 reservoir management for carbon storage: analysis of operational strategies to relieve pressure buildup and improve injectivity. Int. J. Greenh. Gas Control 6, 230–245.

Chadwick, R.A., Noy, D.J., Holloway, S., 2009. Flow processes and pressure evolution in aquifers during the injection of supercritical CO_2 as a greenhouse gas mitigation measure. Petrol. Geosci. 15 (1), 59–73.

Cinar, Y., Bukhteeva, O., Neal, P.R., Allinson, W.G., Paterson, L., 2008. CO_2 Storage in low permeability formations. In: SPE Symposium on Improved Oil Recovery (Tulsa, Oklahoma, USA).

Dietz, D.N., 1965. Determination of average reservoir pressure from build-up surveys. J. Pet. Sci. Eng. 17 (8), 955–959.

Durucan, S., Shi, J.-Q., Sinayuc, C., Korre, A., 2011. In Salah CO_2 storage JIP: carbon dioxide plume extension around KB-502 well–New insights into reservoir behaviour at the in Salah storage site. Energy Proc. 4, 3379–3385.

Eiken, O., Ringrose, P., Hermanrud, C., Nazarian, B., Torp, T.A., Høier, L., 2011. Lessons learned from 14 years of CCS operations: sleipner, in Salah and Snøhvit. Energy Proc. 4, 5541–5548.

Escobar, F.H., Montealegre, M.M., 2008. Determination of horizontal permeability from the elliptical flow of horizontal wells using conventional analysis. J. Pet. Sci. Eng. 61 (1), 15–20.

Garimella, S.S., Ahmed, S., Hossain, M.M., 2019. Comparison of different models for predicting drainage relative permeability using pore scale numerical simulation of supercritical carbon dioxide and brine flow. In: IOP Conference Series: Materials Science and Engineering, vol. 495, 012111.

Goertz-Allmann, B.P., Kühn, D., Oye, V., Bohloli, B., Aker, E., 2014. Combining microseismic and geomechanical observations to interpret storage integrity at the in Salah CCS site. Geophys. J. Int. 198 (1), 447–461.

González-Nicolás, A., Cihan, A., Petrusak, R., et al., 2019. Pressure management via brine extraction in geological CO_2 storage: adaptive optimization strategies under poorly characterized reservoir conditions. Int. J. Greenh. Gas Control 83, 176–185.

Goode, P.A., Thambynayagam, R.K.M., 1987. Pressure drawdown and buildup analysis of horizontal wells in anisotropic media. SPE Form. Eval. 2 (4), 683–697.

Hansen, O., Gilding, D., Nazarian, B., et al., 2013. Snohvit: the history of injecting and storing 1 Mt CO_2 in the fluvial Tubaen Fm. Energy Proc. 37, 3565–3573.

Harp, D.R., Stauffer, P.H., O'Malley, D., et al., 2017. Development of robust pressure management strategies for geologic CO_2 sequestration. Int. J. Greenh. Gas Control 64, 43–59.

Hu, L.W., Bayer, P., Alt-Epping, P., Tatomir, A., Sauter, M., Brauchler, R., 2015. Time-lapse pressure tomography for characterizing CO_2 plume evolution in a deep saline aquifer. Int. J. Greenh. Gas Control 39, 91–106.

Hubbert, M.K., 1953. Entrapment of petroleum under hydrodynamic conditions. AAPG (Am. Assoc. Pet. Geol.) Bull. 37 (8), 1954–2026.

IEAGHG, 2010. Injection Strategies for CO_2 Storage Sites. IEA Greenhouse Gas R&D Programme (IEAGHG).

Lake, J.A., Lomax, B.H., 2019. Plant responses to simulated carbon capture and storage (CCS) CO_2 pipeline leakage: the effect of soil type. Greenh. Gases. 9 (2), 397–408.

Li, Y.L., Han, M.Y., Liu, S.Y., Chen, G.Q., 2019. Energy consumption and greenhouse gas emissions by buildings: a multi-scale perspective. Build. Environ. 151, 240–250.

Liebscher, A., Moller, F., Bannach, A., et al., 2013. Injection operation and operational pressure-temperature monitoring at the CO_2 storage pilot site Ketzin, Germany-Design, results, recommendations. Int. J. Greenh. Gas Control 15, 163–173.

Lipponen, J., Burnard, K., Beck, B., Gale, J., Pegler, B., 2011. The IEA CCS technology roadmap: one year on. Energy Proc. 4, 5752–5761.

Mathias, S.A., McElwaine, J.N., Gluyas, J.G., 2014. Heat transport and pressure buildup during carbon dioxide injection into depleted gas reservoirs. J. Fluid Mech. 756, 89–109.

Mathieson, A., Midgely, J., Wright, I., Saoula, N., Ringrose, P., 2011. In Salah CO_2 Storage JIP: CO_2 sequestration monitoring and verification technologies applied at Krechba, Algeria. Energy Proc. 4, 3596–3603.

Metz, B., Davidson, O., De Coninck, H., Loos, M., Meyer, L., 2005. IPCC Special Report on Carbon Dioxide Capture and Storage. Intergovernmental Panel on Climate Change, Geneva, Switzerland. Technical Report.

Obergassel, W., Arens, C., Hermwille, L., et al., 2018. The Calm before the Storm: an Assessment of the 23rd Climate Change Conference (COP 23). Lawtext Publishing Limited, Bonn.

Osiptsov, A.A., 2017. Fluid mechanics of hydraulic fracturing: a review. J. Pet. Sci. Eng. 156, 513–535.

Rutqvist, J., 2012. The geomechanics of CO_2 storage in deep sedimentary formations. Geotech. Geol. Eng. 30 (3), 525–551.

Sato, K., Horne, R.N., 2018. Time-lapse analysis of pressure transients due to ocean tides for estimating CO_2 saturation changes. Int. J. Greenh. Gas Control 78, 160–167.

Sawada, Y., Tanaka, J., Suzuki, C., Tanase, D., Tanaka, Y., 2018. Tomakomai CCS demonstration project of Japan, CO_2 injection in progress. Energy Proc. 154, 3–8.

Shackley, S., McLachlan, C., Gough, C., 2005. The public perception of carbon dioxide capture and storage in the UK: results from focus groups and a survey. Clim. Pol. 4 (4), 377–398.

Singh, H., 2018. Impact of four different CO_2 injection schemes on extent of reservoir pressure and saturation. Adv. Geo-Energy Res. 2 (3), 305–318.

Tanaka, Y., Abe, M., Sawada, Y., Tanase, D., Ito, T., Kasukawa, T., 2014. Tomakomai CCS demonstration project in Japan, 2014 update. Energy Proc. 63, 6111–6119.

Tanaka, Y., Sawada, Y., Tanase, D., Tanaka, J., Shiomi, S., Kasukawa, T., 2017. Tomakomai CCS demonstration project of Japan, CO_2 injection in process. Energy Proc. 114, 5836–5846.

Van Everdingen, A.F., Hurst, W., 1949. The application of the Laplace transformation to flow problems in reservoirs. J. Petrol. Technol. 1 (12), 305–324.

Wu, Y.-S., Pan, L., 2005. An analytical solution for transient radial flow through unsaturated fractured porous media. Water Resour. Res. 41 (2). https://doi.org/10.1029/2004WR003107.

Yang, D., Doschoris, M., Zhang, L., 2018. Analysis of pressure diffusion-wave fields in matrix-fracture media using Green functions of frequency domain. J. Appl. Phys. 124 (7), 074902.

Yang, F., Bai, B.J., Tang, D.Z., Dunn-Norman, S., Wronkiewicz, D., 2010. Characteristics of CO_2 sequestration in saline aquifers. Petrol. Sci. 7 (1), 83–92.

Zheng, X., Espinoza, D.N., Vandamme, M., Pereira, J.-M., 2022. CO_2 plume and pressure monitoring through pressure sensors above the caprock. Int. J. Greenh. Gas Control 117, 103660.

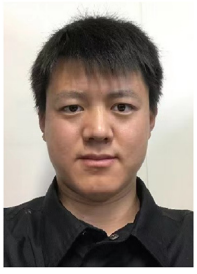

Qiang Sun obtained his BSc and MSc degrees in Shandong University of Science and Technology and China University of Mining and Technology, China, in 2013 and 2016, respectively, and his PhD in Kyushu University, Japan, in 2021. He is doing postdoctoral research at Hainan University, China since 2022. His research interests include (1) experimental investigations on the thermo-hydro-mechanical (THM) behaviors of host rocks for geological storage of CO_2 in saline aquifer and (2) theoretical study and numerical modeling of coupled thermo-hydro-mechanical-chemical (THMC) behaviors in porous media and cap rock system.